

# A Broadside Scanning Substrate Integrated Waveguide Periodic Phase-Reversal Leaky-Wave Antenna

Robert Henry, *Student Member, IEEE*, and Michal Okoniewski, *Fellow, IEEE*

**Abstract**—A broadside-scanning half-mode substrate integrated waveguide periodic leaky-wave antenna architecture with antipodal tapered slots is presented. The antenna builds upon a previously proposed architecture by introducing a periodic phase-reversal of radiating elements. This enables the antenna to operate with a comparatively low substrate permittivity while maintaining grating-lobe-free scanning from reverse to forward endfire.

**Index Terms**—Leaky-wave antenna, periodic phase-reversal, substrate integrated waveguide, traveling wave array.

## I. INTRODUCTION

THE INVENTION of substrate integrated waveguide (SIW) for efficient millimeter (mm)-wave system integration has opened the door to a wealth of new research opportunities. The flexibility of SIW-based systems hinges upon the availability of SIW-compatible components, and thus much effort has been expended to create all kinds of SIW-based devices including antennas. Leaky-wave antennas (LWAs) are traditionally praised for their simple feed mechanism, directive radiation, and frequency-dependent beam scanning. In SIW, many LWAs have been proposed such as the periodic LWA in [1] and the uniform/quasi-uniform LWAs presented in [2] and [3], however none of these antennas offered broadside radiation. Composite right/left-handed (CRLH) LWAs in SIW have therefore received particular interest, offering broad scan ranges in addition to broadside radiation [4]. Recently, it was shown that a half-mode SIW (HMSIW)-based periodic LWA architecture using antipodal tapered slot antenna (ATSA) radiating elements could offer comparable broadside-scanning performance [5]. Using the periodic phase-reversal technique (employed in both [6] and [7] for microstrip-based LWAs), a new architecture of this antenna offering substantially improved design flexibility in terms of its substrate permittivity (up to 55% reduction, in theory) was briefly introduced in [8] and is explored in depth in this letter.

Manuscript received June 13, 2015; accepted July 17, 2015. Date of publication July 29, 2015; date of current version March 04, 2016.

The authors are with the Department of Electrical and Computer Engineering, Schulich School of Engineering, University of Calgary, Calgary, AB T2N 1N4, Canada (e-mail: rjhenry@ucalgary.ca).

Color versions of one or more of the figures in this letter are available online at <http://ieeexplore.ieee.org>.

Digital Object Identifier 10.1109/LAWP.2015.2462733

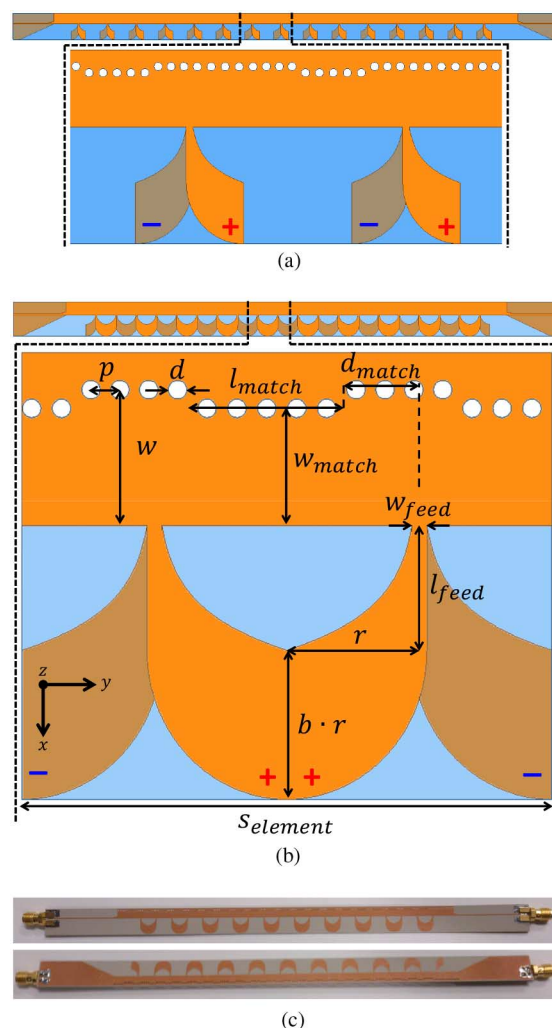


Fig. 1. HMSIW periodic LWA geometries and prototype. (a) Previously proposed “noninverting element” architecture. (b) Proposed “periodic-phase reversal” architecture (length units in mm):  $p = 0.76$ ,  $d = 0.508$ ,  $w = 3.76$ ,  $l_{\text{match}} = 4.12$ ,  $w_{\text{match}} = 3.24$ ,  $d_{\text{match}} = 2.14$ ,  $w_{\text{feed}} = 0.42$ ,  $l_{\text{feed}} = 3.42$ ,  $r = 3.86$ ,  $b = 1.06$ ,  $s_{\text{element}} = 14.58$ ,  $\epsilon_{rz} = 10.96$ ,  $\epsilon_{rx} = \epsilon_{ry} = 13.3$ . (c) Antenna prototype (top and bottom perspectives).

## II. PROPOSED ANTENNA

### A. Antenna Architecture

The antenna architecture can be viewed as an HMSIW feeding 20 periodically spaced ATSA elements. The previously proposed architecture from [5] is shown in Fig. 1(a) (hereby

referred to as the “noninverting element design”) in order to help clarify the “periodic phase-reversal” architecture shown in Fig. 1(b) (with phase-reversal indicated by the  $+/-$  signs).

### B. Periodic Phase-Reversal Principle of Operation

The periodic phase-reversal of adjacent ATSA elements introduces a frequency-independent  $180^\circ$  phase shift per unit cell from a radiated-fields perspective. This allows the element feed spacing to be reduced by  $180^\circ$  at the broadside frequency while maintaining similar beam-scanning performance to the noninverting element design. The reduced electrical spacing between elements can allow the substrate permittivity to be reduced (assuming linear scaling of the antenna dimensions) while maintaining grating-lobe-free scanning [6]. In contrast to the periodic phase-reversal LWAs in [6] and [7], the proposed antenna is inherently SIW-compatible and offers maximum radiation in the plane of the substrate.

## III. ANTENNA DESIGN

### A. Substrate, Antenna Excitation, and HMSIW Design

The antenna was fabricated using a 0.64-mm-thick Rogers 3210 substrate with anisotropic substrate permittivity values shown in Fig. 1(b), which were obtained through Rogers directly. The HMSIW used to feed the ATSA elements is defined by parameters  $w$ ,  $d$ , and  $p$  shown in Fig. 1(b), values for which were approximated using design equation from [9] for an X-band waveguide. An approximate cutoff frequency of 6.2 GHz was observed in simulations, which enabled operation in the 8–12 GHz range. The antenna was excited by a tapered 50- $\Omega$  microstrip [10], and the ground plane was tapered to allow the introduction of the ATSA elements from the open HMSIW sidewall.

### B. Radiating Element Design and Broadside Open-Stop Band Mitigation

The radiating element geometry is fully defined by parameters  $w_{\text{feed}}$ ,  $l_{\text{feed}}$ ,  $r$ , and axial ratio  $b$  shown in Fig. 1(b). These parameters were optimized in designing the noninverting element antenna in order to achieve a broad scan range in the substrate plane and a weak loading on the guided HMSIW mode as was explained in depth in [5]. Parameter  $r$  was given some flexibility in the new periodic phase-reversal design to ensure adjacent ATSA elements would contact, as it was observed that small gaps degraded the simulated radiation pattern.

Periodic LWAs are well known to exhibit an open-stop band at the broadside scan angle frequency, however it was eliminated in [5], [11], and [12] by matching the unit cell at the broadside frequency. The same technique was applied to the new periodic phase-reversal antenna. An optimization was executed that ensured element parameter  $r$  was valued such that adjacent ATSA elements would contact, while matching section parameters  $w_{\text{match}}$ ,  $l_{\text{match}}$ ,  $d_{\text{match}}$ , and unit-cell length  $s_{\text{element}}$ , were varied to acquire a minimum 30 dB return loss at the broadside frequency (9.6 GHz), while maintaining a  $180^\circ$  phase shift between radiating elements.

The efficacy of the technique used can be viewed in the Bloch impedance of the periodic structure (calculated using

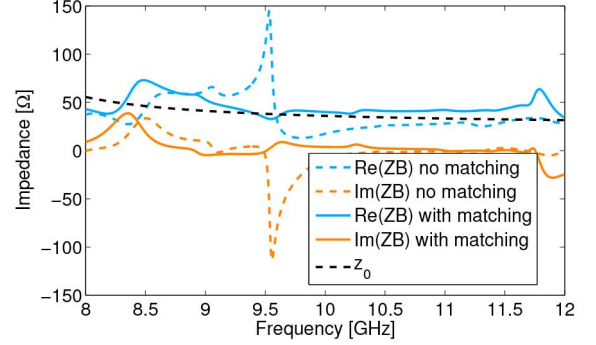


Fig. 2. Bloch impedance for a six-unit-cell structure with (—) and without (---) matching sections.

a six-unit-cell simulation and equations from [13]) shown in Fig. 2. Passband operation occurs when the Bloch impedance is matched to the real valued source and termination impedance, which is the waveguide impedance. It is shown in Fig. 2 that the addition of the unit-cell matching section greatly improved the Bloch impedance match to the waveguide impedance (extracted from HFSS waveport solutions) at the broadside frequency (9.6 GHz), which was reflected in the acceptable return loss of the 20-unit-cell structure reported in Fig. 4.

### C. Prototype Fabrication

Three prototypes were fabricated using a photolithography-based process [one of which is shown in Fig. 1(c)] in order to observe the impact of fabrication constraints on repeatability. In particular, the process had a  $+/-3$ -mil drill placement accuracy, which was a concern due to via spacings as small as 10 mils in the design. Also, correspondence with Rogers indicated that the quoted substrate  $xy$ -plane relative permittivity (13.3) does not account for any  $xy$  anisotropy, thus leading to some inaccuracy in the simulation model.

## IV. EXPERIMENTAL VALIDATION

### A. Leaky-Wave Analysis

Measured leaky wavenumbers ( $k_{\text{LW}} = \beta_{-1} - j\alpha$ , where  $\beta_{-1}$  is the phase constant of the  $n = -1$  space harmonic and  $\alpha$  is the mode attenuation coefficient) for the three prototype antennas are shown in Fig. 3 and are compared to the simulated leaky wavenumber. One prototype is used in subsequent measurements (labeled  $\beta_{-1}$  Measured in Fig. 3). Leaky wavenumbers were measured by using TRL calibration to remove the connectors, and standard deembedding techniques along with simulated data for removing the microstrip-to-HMSIW transitions. Periodic analysis [13] was then applied to the resulting 20-unit-cell measurements to compute the wavenumber at each frequency. Similarly, the simulated wavenumber was calculated using 20-unit-cell simulated data in order to yield the best comparison.

### B. Impedance Bandwidth

The measured and simulated antenna  $S$ -parameters are presented in Fig. 4. The measured antenna impedance bandwidth extended from 8.4 to 11.8 GHz (34%).

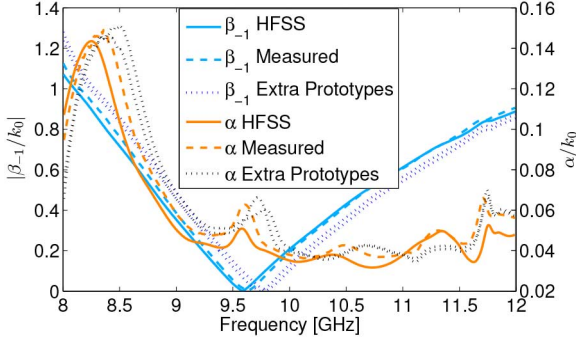


Fig. 3. Measured (three prototypes) and simulated normalized leaky wavenumbers  $k_{LW}$ .

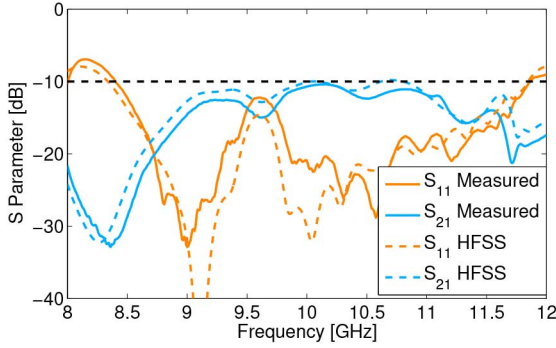


Fig. 4.  $S$ -parameters used to define impedance bandwidth.

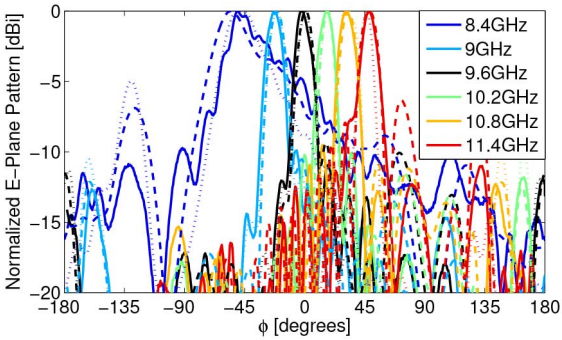


Fig. 5. Normalized E-plane radiation pattern [dBi]: Measured (—), Simulated (---), and Theoretical (-----).

### C. Radiation Pattern

Considering the coordinate system shown in Fig. 1(b), let us define a spherical coordinate system with the  $+y$ -direction as the zenith,  $\phi$  as the polar angle, and  $\theta$  as the azimuthal angle, both measured from  $+x$ . Using this coordinate system, the antenna has primarily  $\phi$ -directed linear polarization. Copolarized normalized E-plane ( $xy$ -plane) radiation patterns for a sample of frequencies are shown in Fig. 5. The theoretical patterns were calculated using the simulated leaky wavenumber (shown in Fig. 3) to compute an array factor for the antenna [14], which was multiplied by the simulated element pattern. Corresponding simulated H-plane patterns are shown in Fig. 6. The E- and H-plane patterns constitute a frequency-dependent scanning, fan-shaped beam with maximum radiation in the plane of the substrate.

The main beam angle of the antenna can be calculated using the leaky-wave phase constant in conjunction with the well-

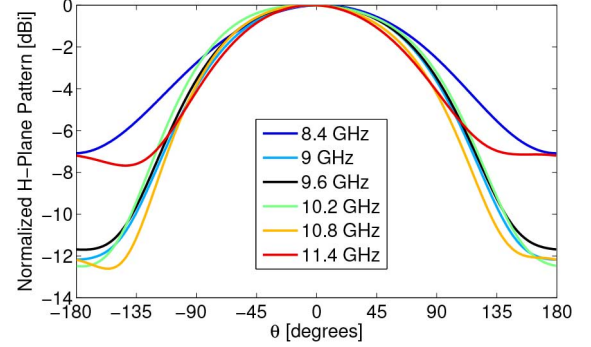


Fig. 6. Simulated normalized H-plane antenna radiation pattern [dBi].

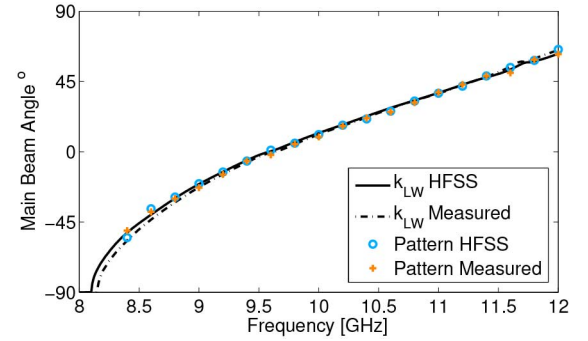


Fig. 7. Main beam scan angle.

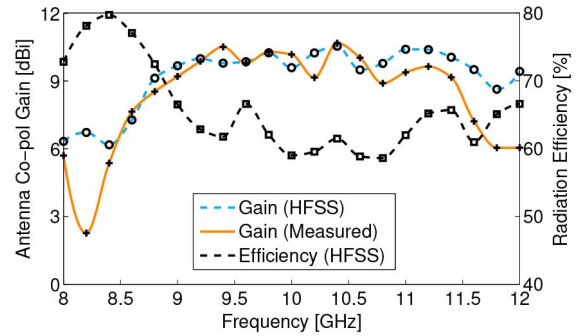


Fig. 8. Antenna gain and efficiency versus frequency.

known relation  $\phi_m = \sin^{-1}(\frac{\beta_{-1}}{k_0})$ . Results of this computation are shown in Fig. 7 for both measured and simulated leaky wavenumbers and are compared to measured and simulated pattern main beam angles.

### D. Antenna Gain and Efficiency

The antenna gain is reported as a function of frequency in Fig. 8. The simulated efficiency is also shown where power dissipated in the matched load was included as part of the accepted power. Reflected power was excluded from the calculation (as is customary).

### E. Permittivity Reduction Results

As mentioned, the new periodic phase-reversal architecture enables a reduction in the substrate permittivity while maintaining grating-lobe-free scanning. To illustrate this point, both the noninverting element design and the new periodic phase-reversal design were scaled in simulations, and the substrate per-



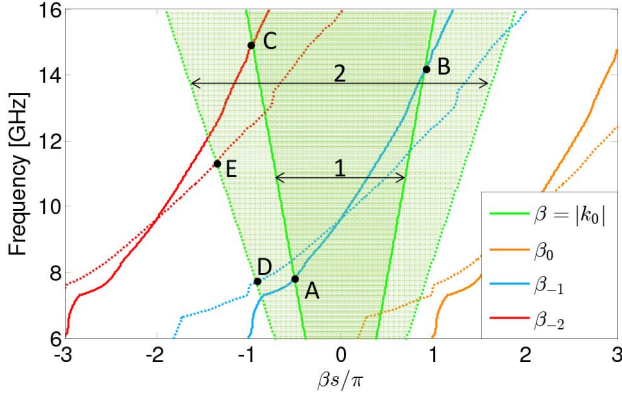


Fig. 9.  $\epsilon_r = 6.15$  dispersion curves: Periodic phase-reversal design (—), Noninverting element design (---).

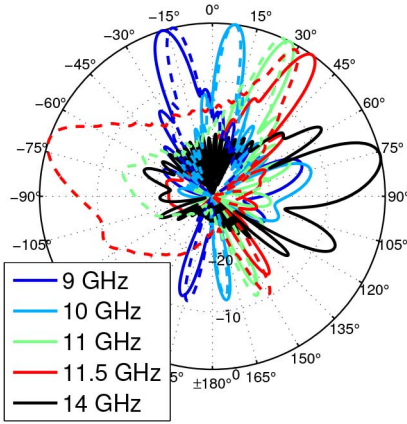


Fig. 10.  $\epsilon_r = 6.15$  normalized radiation patterns [dBi]: Periodic phase-reversal design (—), Noninverting element design (---).

mittivity was changed to  $\epsilon_r = 6.15$ . The simulated dispersion curves for relevant Floquet modes (space harmonics) for both antennas are shown in Fig. 9. Region 1 indicates the fast wave (radiating) region for the periodic phase-reversal antenna, and region 2 indicates the fast wave (radiating) region for the noninverting element design. It was observed that the dispersion curves for the phase-reversal architecture shift by a factor of  $\pi$  and approximately double in slope. This allows the  $n = -1$  space harmonic to scan the full space (between points A and B) before the  $n = -2$  space harmonic becomes fast and radiating at point C. In contrast, the noninverting element design's  $n = -1$  space harmonic begins to radiate at point D and can only scan until point E without the appearance of grating lobes. Point E corresponds to the frequency at which the  $n = -2$  space harmonic becomes fast and radiating. This was observed in the simulated radiation patterns of the  $\epsilon_r = 6.15$  scaled structures shown in Fig. 10, where it is seen that the pattern for the noninverting element design suffers from a reverse endfire grating

lobe at 11.5 GHz, while the phase-reversal architecture can scan to forward endfire (14 GHz) without the appearance of grating lobes.

## V. CONCLUSION

The most recent results from the study of a new HMSIW periodic phase-reversal leaky-wave antenna have been presented. The design offers broadside scanning performance and can be implemented on a lower-permittivity substrate than the previously proposed noninverting element design.

## REFERENCES

- [1] F. Xu, K. Wu, and X. Zhang, "Periodic leaky-wave antenna for millimeter wave applications based on substrate integrated waveguide," *IEEE Trans. Antennas Propag.*, vol. 58, no. 2, pp. 340–347, Feb. 2010.
- [2] J. Liu, D. Jackson, and Y. Long, "Substrate integrated waveguide (SIW) leaky-wave antenna with transverse slots," *IEEE Trans. Antennas Propag.*, vol. 60, no. 1, pp. 20–29, Jan. 2012.
- [3] J. Xu, W. Hong, H. Tang, Z. Kuai, and K. Wu, "Half-mode substrate integrated waveguide (HMSIW) leaky-wave antenna for millimeter-wave applications," *IEEE Antennas Wireless Propag. Lett.*, vol. 7, pp. 85–88, 2008.
- [4] Y. Dong and T. Itoh, "Composite right/left-handed substrate integrated waveguide and half mode substrate integrated waveguide leaky-wave structures," *IEEE Trans. Antennas Propag.*, vol. 59, no. 3, pp. 767–775, Mar. 2011.
- [5] R. Henry and M. Okoniewski, "A broadside-scanning half-mode substrate integrated waveguide periodic leaky-wave antenna," *IEEE Antennas Wireless Propag. Lett.*, vol. 13, pp. 1429–1432, 2014.
- [6] N. Yang, C. Caloz, and K. Wu, "Full-space scanning periodic phase-reversal leaky-wave antenna," *IEEE Trans. Microw. Theory Tech.*, vol. 58, no. 10, pp. 2619–2632, Oct. 2010.
- [7] S. Paulotto, P. Baccarelli, and D. Jackson, "A self-matched wide scanning U-stub microstrip periodic leaky-wave antenna," *J. Electromagn. Waves Appl.*, vol. 28, no. 2, pp. 151–164, 2014.
- [8] R. Henry and M. Okoniewski, "Half mode substrate integrated waveguide periodic leaky wave antenna with antipodal tapered slots," in *Proc. IEEE Antennas Propag. Soc. Int. Symp.*, Jul. 2014, pp. 1284–1285.
- [9] F. Xu and K. Wu, "Guided-wave and leakage characteristics of substrate integrated waveguide," *IEEE Trans. Microw. Theory Tech.*, vol. 53, no. 1, pp. 66–73, Jan. 2005.
- [10] D. Deslandes, "Design equations for tapered microstrip-to-substrate integrated waveguide transitions," in *Proc. IEEE MTT-S Int. Microw. Symp.*, May 2010, pp. 1–1.
- [11] S. Paulotto, P. Baccarelli, F. Frezza, S. Member, and D. R. Jackson, "A novel technique for open-stopband suppression in 1-D periodic printed leaky-wave antennas," *IEEE Trans. Antennas Propag.*, vol. 57, no. 7, pp. 1894–1906, Jul. 2009.
- [12] T. Cameron, A. Sutinjo, and M. Okoniewski, "A circularly polarized broadside scanning patch array," in *Proc. 4th EuCAP*, Apr. 2010, pp. 1–3.
- [13] R. Collin, *Foundations for Microwave Engineering*, 2nd ed. New York, NY, USA: McGraw-Hill, 1992, ch. 8.
- [14] C. Caloz and T. Itoh, "Array factor approach of leaky-wave antennas and application to 1-D/2-D composite right/left-handed (CRLH) structures," *IEEE Microw. Wireless Compon. Lett.*, vol. 14, no. 6, pp. 274–276, Jun. 2004.